JOURNAL OF SYNCHROTRON RADIATION

ISSN 1600-5775

Absolute intensity calibration for carbon-edge soft X-ray scattering

Thomas Ferron,[a] Devin Grabner,[a] Terry McAfee[a,b] and Brian Collins[a]*

[a]Department of Physics and Astronomy, Washington State University, Pullman, WA 99163, USA, and [b]Advanced Light Source, Lawrence Berkeley National Laboratory, Berkeley, CA, USA. *Correspondence e-mail: brian.collins@wsu.edu

Received 1 June 2020
Accepted 11 August 2020

Edited by S. M. Heald, Argonne National Laboratory, USA

Keywords: resonant soft X-ray scattering; absolute scattering intensity; detector calibration.

Resonant soft X-ray scattering (RSOXS) has become a premier probe to study complex three-dimensional nanostructures in soft matter through combining the robust structural characterization of small-angle scattering with the chemical sensitivity of spectroscopy. This technique borrows many of its analysis methods from alternative small-angle scattering measurements that utilize contrast variation, but thus far RSOXS has been unable to reliably achieve an absolute scattering intensity required for quantitative analysis of domain compositions, volume fraction, or interfacial structure. Here, a novel technique to calibrate RSOXS to an absolute intensity at the carbon absorption edge is introduced. It is shown that the X-ray fluorescence from a thin polymer film can be utilized as an angle-independent scattering standard. Verification of absolute intensity is then accomplished through measuring the Flory–Huggins interaction parameter in a phase-mixed polymer melt. The necessary steps for users to reproduce this intensity calibration in their own experiments to improve the scientific output from RSOXS measurements are discussed.

1. Introduction

Characterizing morphology in composite soft matter systems is vital to unraveling the origins of their unique properties. Advances in molecular synthesis have allowed for the development of macromolecules capable of exhibiting advantageous behaviors that have been utilized in organic electronics (Cui *et al.*, 2019; Liang *et al.*, 2020), bottom-up nanolithography (Zhang, 2003), and drug delivery (Hinde *et al.*, 2017). Along with requiring increasingly complex molecular architectures, advances in soft matter technologies are consistently tied to molecular assembly into an ideal nanostructure. In polymer photovoltaics, it is found that the interplay between crystallinity and miscibility of donor/acceptor molecules results in a plethora of different nanostructures (Ye *et al.*, 2018), many of which depend on processing conditions, and dramatic morphological variation can be found even within a single material system (Feng *et al.*, 2020; Collins *et al.*, 2013). In electrochemical transistors, balancing the size and composition of charge conducting domains dispersed within a matrix of ionic channels allow for fabricating biological sensors with high transconductance (Rivnay *et al.*, 2016). In micelle drug delivery platforms, the concentration of therapeutic molecules within the nanocarrier core domains is critical to next-generation smart medicine (Zhang *et al.*, 2011). All of these applications depend on measuring not only structure but also the chemical composition within that structure, ideally without laborious and disruptive chemical labeling. Without established techniques capable of such measurements, it becomes impossible to understand the vital structure–function relationships found in soft matter.

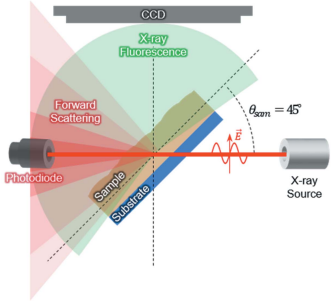

One such technique that has shown promising sensitivity to the molecularly mixed nanodomains found in soft matter is resonant soft X-ray scattering (RSOXS). RSOXS combines the chemical sensitivity of near-edge X-ray absorption fine-structure (NEXAFS) spectroscopy with the nano-to-meso-scale characterization afforded to small-angle scattering (SAS) (Ade & Hitchcock, 2008; Carpenter *et al.*, 2015; Ferron *et al.*, 2017). Where traditional SAS experiments, using either hard X-rays or neutrons, measure elastically scattered radiation to probe density inhomogeneities within a sample, RSOXS is capable of distinguishing domains based on their chemical makeup. This is accomplished by tuning the X-ray energy at, or nearby, an elemental absorption edge corresponding to the transition of a core-electron into an unoccupied molecular orbital (Stöhr, 1992). The strength and position of such transitions greatly depends on intramolecular bonding arrangements of a given molecule and is represented as the complex index of refraction $n(E) = 1 - \delta(E) + i\beta(E)$. The index varies dramatically over an absorption edge due to these transitions and is directly related to the scattering intensity from domains i and j through the unitless contrast function $C(E) = |\Delta n_{ij}(E)|^2$. These transitions afford RSOXS intrinsic chemical contrast which, unlike neutron scattering, require no chemical modification. Throughout this article, expressions that are commonly associated with scattering length density (ρ_i) will be converted into $n(E)$ using the relationship $n(E) = \lambda^2/2\pi\ \rho(E)$.

SAS experiments, including RSOXS, provide a statistically relevant survey of a probed nanostructure, and interpretations of the resulting dataset often follow a common path. Scattering data are represented as an intensity versus momentum transfer wavevector $q = 4\pi/\lambda \sin\theta$, where λ is the photon wavelength and θ is the scattering angle. The statistics of size and structure of domains within a population can be determined through the shape of a scattering profile (Roe, 2000) When the data are presented on an arbitrary scale, the user is limited to analyze the q-dependence of scattering or apply intensity-free models such as a Guinier analysis (Guinier & Fournet, 1955). However, a wealth of information regarding phase composition, volume fraction, or surface area occupied by the scattered domains is lost without a calibration to an absolute unit (Wignall & Bates, 1987; Zhang *et al.*, 2010).

Scattering on an absolute scale is described by the differential scattering cross section $\mathrm{d}\Sigma/\mathrm{d}\Omega$. This value represents the probability that a particle will be scattered per unit volume per unit time toward a region of space denoted by a unit solid angle normalized to the incident particle flux. Experimentally, this value can be calculated as a function of q and the photon energy, E, through the relationship (Spalla *et al.*, 2003; Allen *et al.*, 2017)

$$\frac{\mathrm{d}\Sigma}{\mathrm{d}\Omega}(q, E) = \frac{I_s(q, E)}{I_0(0, E)}\left[\frac{1}{T(E)\, t_s \Omega}\right], \qquad (1)$$

where $I_s(q,E)$ is the scattered intensity, $I_0(0,E)$ is the incident X-ray flux, $T(E)$ is the transmittance of the sample and substrate assembly, t_s is the sample thickness, and Ω is the differential solid angle subtended by the detector. When properly normalized, $\mathrm{d}\Sigma/\mathrm{d}\Omega$ has units of cm^{-1}.

To date, most RSOXS experiments have only utilized intensity on an arbitrary scale. This is in part due to the current absolute scattering calibration techniques and standards being unsuitable for RSOXS measurements. There are two common techniques that modern SAS instruments use to calibrate measurements to an absolute intensity. The first method, known as a primary calibration, is to simply normalize the scattered intensity to a direct measurement of the incident flux using the same photodetector (Dreiss *et al.*, 2006; Allen *et al.*, 2017). This method is simple in principle, but many detectors, including those at the RSOXS beamlines, are not equipped with the dynamic range necessary to measure both the direct flux from a synchrotron in addition to sample scattering. The alternative method, known as a 'secondary calibration', uses a pre-characterized standard with a known scattering cross section to match an instrument intensity to a calibrated intensity curve (Orthaber *et al.*, 2000); an example would be a slab of glassy carbon [NIST SRM 3600 (Allen *et al.*, 2017)] used in both high flux and tabletop sources. Unfortunately, the available standards are far too thick (on the order of millimetres) for soft X-rays to penetrate, making them unsuitable for RSOXS to use. Finding an alternative method to achieve absolute intensity calibration that is both widely accessible and easily implemented would drastically improve the potential knowledge gained from RSOXS measurements.

Previously, we have shown that a suitable candidate for RSOXS intensity calibration is a parasitic background intensity originating from X-ray fluorescence (XRF) (Ferron *et al.*, 2017). In practice, measured RSOXS signals are a convolution of two types of photon emission, scattering and XRF. XRF is an isotropic emission that results from the relaxation of an electron following a core vacancy, and the intensity can be modeled using the equation (Bearden, 1967; Krause & Oliver, 1979)

$$I_{\mathrm{XRF}}(E) = \omega\, A(E)\, \Omega^{-1}, \qquad (2)$$

where $I_{\mathrm{XRF}}(E)$ is the flux normalized intensity of the XRF in units of sterad^{-1} (inverse steradian), ω is the quantum efficiency of the emission process, $A(E)$ is the fraction of absorbed photons, and Ω^{-1} is the solid angle as defined previously. If we assume that only fluorescence from the $C_{K\alpha}$ transition will be present in our signal (with a known quantum efficiency of $\omega_{C_{K\alpha}} = 0.002525$ and photon energy $E_{\mathrm{XRF}} = 277$ eV) (Hubbell *et al.*, 1994) and that the emitted light is isotropic with no appreciable self-attenuation ($\Omega = 4\pi$), only the photo-absorbance $A(E)$ needs to be measured for an intensity calibration using $I_{\mathrm{XRF}}(E)$. In our previous work, we had assumed that our measured RSOXS signal would decay as $q \rightarrow \infty$ as a power-law and eventually be overtaken by XRF. This gave us a quantitative measurement of the scattering invariant for a series of copolymers allowing for a calculation of domain volumes. However, fitting the XRF from the edge of a detector was convoluted with scattering and required a known decay profile. The nanostructures under investigation also scattered out to relatively high angles, making it a non-

ideal sample for calibration. Finding a suitable calibration alternative to achieve an absolute intensity calibration that is both widely accessible and easily implemented would drastically improve the potential knowledge gained from RSOXS measurements.

In this contribution, we present a facile method to calibrate carbon-edge RSOXS to an absolute intensity using XRF from a polymer film. This calibrates the relative responsivity between the detectors responsible for measuring incident and scattered signals and results in an absolute scattering cross-section measurement for this critical absorption edge for molecular materials. We use this method to calibrate the detectors at the RSOXS instrument in beamline 11.0.1.2 of the Advanced Light Source (ALS) at Lawrence Berkeley National Laboratory. We then verify that absolute intensity has been achieved by demonstrating the measurement of the Flory–Huggins interaction parameter of polystyrene and poly(methyl methacrylate) using Leibler's scattering theory, which requires an absolute intensity to properly characterize the polymer melt. The accuracy, availability, and simplicity of such a technique along with our choice of calibrant will be discussed along with an outline of steps required for users to reproduce our methods. This method can be used at most multidetector beamlines interested in probing at the carbon absorption edge and could be extended to other elemental absorption edges with the appropriate thin films.

2. Materials and sample preparation

Pure polystyrene was chosen as the calibrant polymer as it is fairly robust to radiation damage, ambient oxidation, and contains minimal nanostructure that might cause a scattering signal. Additionally, it has an attenuation length of 5 µm at E_{XRF} (compared with 0.2 µm at 320 eV, above the absorption edge) justifying our earlier assumption of negligible self-absorption of fluorescence (Henke *et al.*, 1993). The polystyrene used in this study was purchased from Polymer Source (MW = 21.5 kDa, PDI = 1.3) and used without further purification. Thin films were fabricated by spin-coating (1500 r.p.m. for 20 s) solutions of 2–4 wt% polymer dissolved in toluene (Sigma Aldrich, 99.9%) directly onto silicon nitride substrates (2 mm × 2 mm window, 100 nm-thick, Norcada). Samples were kept in a nitrogen environment until being transferred into the scattering chamber for X-ray measurements. Copolymers of poly(styrene-block-methyl methacrylate) (PS-b-PMMA) used for confirmation of absolute intensity calibration were purchased from Polymer Source (MW_{PS} = 13 kDa, MW_{PMMA} = 13 kDa, PDI = 1.10, syndiotactic >78%) and used without further purification. Copolymers were dissolved in toluene at 1 wt% and spuncast (1500 r.p.m., 20 s) onto pre-cleaned silicon substrates (15 min consecutive baths of 2-propanol and acetone followed by a 15 min exposure to a UV ozone) coated with an approximate 20 nm layer of sodium polystyrene-sulfonate (Na-PSS). Polymer thin films were then floated in deionized water using Na-PSS as a sacrificial layer and mounted on silicon nitride windows. Substrates were then annealed in a nitrogen glovebox (O_2 < 0.1 p.p.m., H_2O < 0.1 p.p.m.) at 140°C for 24 h and subsequently quenched to room temperature.

3. X-ray measurements and data reduction

All X-ray measurements were conducted at beamline 11.0.1.2 at the Advanced Light Source. Details regarding the beamline optics have been reported previously (Gann *et al.*, 2012). Samples are exposed to monochromatic light with photon energy varied over the carbon absorption edge (270 eV to 340 eV, energy resolution ∼100 meV) where the resulting signal (scattering or fluorescence) is captured with a CCD area detector (Princeton Instruments PI-MTE), recorded in units of analog-to-digital units (ADU). The sample-to-detector distance is measured with aggregate 100 nm polystyrene spheres (Gann *et al.*, 2012) placed at the axis of rotation of the sample stage (verified through θ–2θ reflections off the silicon nitride frame) and determined to be 57.6 mm. RSOXS measurements was conducted in a standard transmission geometry. Incident flux normalization is accomplished through a pair of detectors including a GaAs photodiode located within the scattering chamber and a gold mesh upstream from the sample.

Dual flux monitors are designed to allow active corrections to the incident beam intensity during data collection. Fig. 1(*a*) gives a basic scheme of how this strategy works in practice. The incident flux as a function of energy is measured with the photodiode current, $J_{PD}(E)$, while the upstream gold mesh is simultaneously monitoring the intensity through a drain current, $J_{Au}(E)$. The ratio between these two monitors acts as a correction factor, $I_{CF}(E) = J_{PD}(E)/J_{Au}(E)$, allowing one to calculate the expected flux, as measured on the photodiode, given a measurement of $J_{Au}(E)$ during RSOXS (or XRF) data collection. In order for this active intensity monitor to work, the spectral character of $I_{CF}(E)$ must be constant during the duration of a single measurement. Normalization of XRF data in this study is accomplished with an average $I_{CF}(E)$ calculated from direct beam measurements immediately prior to and following data collection. Fig. 1(*b*) presents a typical averaged spectrum of $I_{CF}(E)$ and the standard deviation between the two measurements is given by the shaded region. Note that the features in $I_{CF}(E)$ originate from large dips in both $J_{PD}(E)$ and $J_{Au}(E)$ due to carbon contamination on the beamline optical elements – the details of which can change with time as the beam on the optics drift or as the contamination level changes. Our ability to monitor the direct flux is limited by this drift in $I_{CF}(E)$ that can occur during data collection and in this study varied by as much as 7% during data collection. The uncertainty introduced by this instability in $I_{CF}(E)$ defines the lower bound to the accuracy of any absolute intensity calibration. Nominally, the authors note that a persistent and sometimes random drift can be found in the direct flux over the duration of an average beam time and we recommend that $I_{CF}(E)$ is recorded before and after any measurement where absolute intensity is desired.

XRF measurements are conducted in a detector geometry schematically outlined in Fig. 2. The current capabilities of

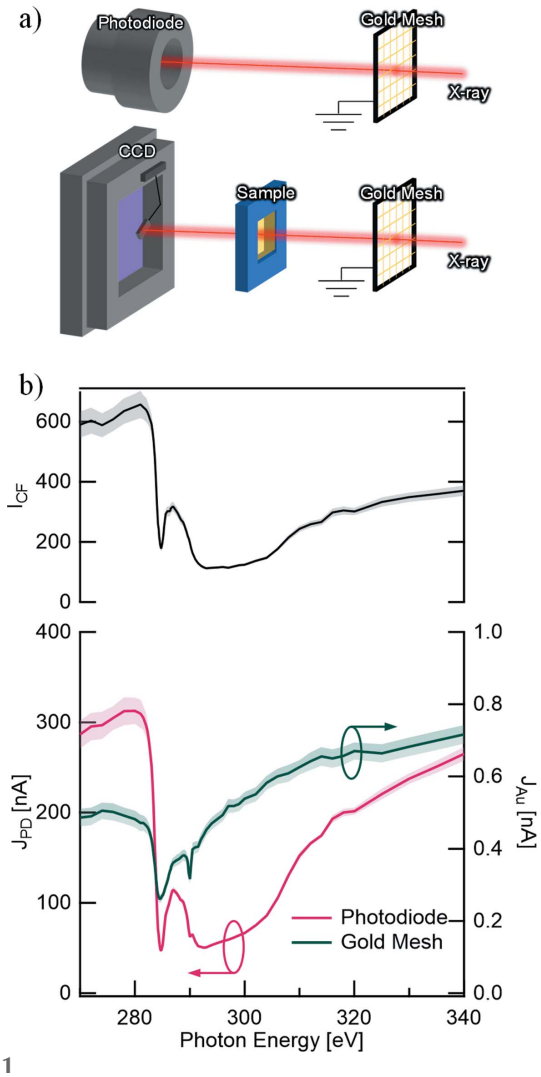

Figure 1
(*a*) Scheme to monitor incident flux during data collection. A description is given in the main text. (*b*) Example spectrum of an average $I_{CF}(E)$ (black), with corresponding $J_{PD}(E)$ (red) and $J_{Au}(E)$ (green), acquired before and after RSOXS measurements. The standard deviation of the two measurement is represented by the shaded region.

the beamline allow measurements of the XRF intensity and sample transmittance to be taken sequentially, both of which are required to calculate the detector responsivity from equation (2). The geometry in Fig. 2 proposes how the experiment can be run simultaneously given a second photodiode mounted independently from the CCD detector; this would help reduce the lower limit of our uncertainty discussed previously. The transmittance can be calculated by measuring the X-ray flux on the photodiode with and without the sample in the path of the beam. The corresponding absorption spectra can be modeled according to Beer's law, $I(E)/I_0(E) = \exp[-\mu(E)\rho t] \equiv 1 - A(E)$, where $I(E)$ and $I_0(E)$ is the photodiode current measured with and without the sample, respectively, $\mu(E)$ is the mass absorption coefficient ($cm^2\ g^{-1}$) acquired from the CXRO database off resonance (Henke *et al.*, 1993), $\rho = 1.04\ g\ cm^{-3}$ is the mass density of polystyrene, and t is the sample thickness (nm) which, if unknown, can be determined. In this study $I_0(E)$ is a measure of the direct beam

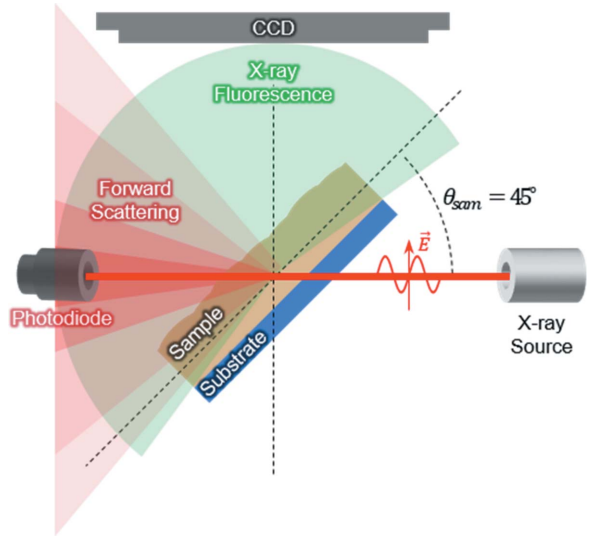

Figure 2
Experimental schematic to potentially simultaneously measure photoabsorption (transmittance) and X-ray fluorescence. Vertically polarized X-rays are incident on the sample rotated to 45°. The forward placed photodiode allows for a measure of $A(E)$, when compared with the incident flux, and the CCD can detect the isotropic XRF emission. The CCD detector is rotated by 90° to limit scattering signal that may otherwise contaminate the XRF signal.

and the substrate absorption is included in $\mu(E)$ as depicted in Fig. 1(*a*) (Collins & Ade, 2012). From Beer's law we can define $A(E)$ as the fraction of absorbed photons used in fluorescence calculations. XRF can be measured by rotating the CCD by 90° from its forward position – any scattering from the calibration sample will miss the CCD detector. The X-ray polarization is additionally chosen to be perpendicular to the CCD direction to further reduce potential scattering toward the detector not resulting from fluorescence. Lastly, the sample is rotated by 45° to increase the exposure of XRF photons to the CCD, while maintaining the full area of the beam passing through the sample.

Images collected on the CCD are reduced to an XRF intensity through the following relationship,

$$I'_{XRF}(E) = \Omega^{-1}\left\{\frac{\left[S_{film}(E,t) - S_{dark}(t)\right]}{J_{Au}(E)\, I_{CF}(E)\, t} - \frac{\left[S_{empty}(E,t) - S'_{dark}(t)\right]}{J'_{Au}(E)\, I_{CF}(E)\, t'}\right\}, \quad (3)$$

where $I'_{XRF}(E)$ is the uncalibrated XRF intensity, $S_x(E,t)$ is the signal measured by the CCD (in units of ADU) from the sample, an empty substrate, and with the shutter closed (subscripts 'film', 'empty', and 'dark', respectively), $J_{Au}(E)$ is the mesh drain current measured during data collection, $I_{CF}(E)$ is the average correction factor from before and after XRF measurements, $\Omega = 2.2 \times 10^{-7}$ sterad is the solid angle associated with a single pixel (with pixel dimensions 0.27 mm × 0.27 mm), and t is the exposure time. Terms marked with a prime were taken alongside the empty substrate measurement. The pre-calibrated units of

equation (3) are in ADU/(nA s sterad). XRF exposures are set to 20 s per energy to optimize signal while limiting radiation exposure. Dark images with equal exposure times are subtracted pixel-by-pixel from light images and subtracted images are then flattened due to the different unit solid angle associated with each pixel relative position to the sample. We use a polynomial fit to an azimuthal averaged profile and normalize to the central pixel. On average, the intensity at the edge of the detector is found to be 2–3% lower than the central pixel. The flattened curve is then averaged, and a standard error is calculated for each frame due to the distribution in pixel readout.

Verification of final calibration was accomplished via temperature-dependent RSOXS acquired in a transmission geometry using a Peltier cooled sample stage. Sample temperatures were slowly ramped starting with 10°C increments and reduced to 5°C when approaching the glass transition temperature T_g of the polymers. Upon reaching the desired temperature, samples were soaked for approximately 5 min to equilibrate before collecting data. All data were reduced using the *NIKA* software package with built-in RSOXS instrument support (Ilavsky, 2012). Profile fits utilized the Levenberg–Marquardt fitting algorithm within *IGOR Pro* (v8.04) with a custom fit function following the methods outlined in this paper.

4. Intensity calibration results

Fig. 3(*a*) gives the measured fluorescence of three polystyrene films of increasing thickness. All samples exhibit an identical spectral profile with expected variations in intensity as a result of increased absorbance found in thicker films. We can immediately discern the origin of the signal to be from XRF instead of scattering due its similar spectral shape to that of a polystyrene NEXAFS absorption profile (Ade & Hitchcock, 2008). To further verify that this signal is not from scattering, Fig. 3(*b*) shows a direct comparison of the measured fluorescence compared with the RSOXS profiles of one of the samples. At all energies, RSOXS is higher than XRF and asymptotically drops to the XRF level with increasing q value. At higher energies it is apparent that the scattering itself becomes overwhelmed by a background fluorescence, but the two signals are still easily distinguishable. This exercise shows that when the RSOXS signal is calibrated to an absolute scale it becomes possible to subtract the XRF background using equation (2).

Qualitative differences can be seen in the measured XRF near 285.1 eV corresponding to the C=C π^* resonance. The relative intensity between the peak height and other spectral features decreases as sample thickness is increased. We attribute this overall reduction in intensity to a breakdown of the polystyrene due to beam damage. A previous investigation into chemical transformations caused by soft X-ray exposure has suggested that a common damage pathway in polystyrene is for the carbon double bonds within the aromatic ring to become saturated with abstracted hydrogen from the backbone. This breakdown in the ring structure subsequently leads to a reduction in the π^* resonance and an increase in the σ manifold, the exact behavior we see in our thickest sample (Wang *et al.*, 2009). In our experiments, the photo-absorption $A(E)$ was always measured prior to the XRF and at the same location on the film to ensure an identical sample volume. Therefore, any beam damage that may have occurred while acquiring $A(E)$ will impact the XRF spectra. For this reason, all fits to the XRF data only included data above the π^* resonance to minimize the influence of beam damage.

Calculating the calibration factor to convert RSOXS to an absolute intensity is now accomplished by fitting the intensity of the CCD-based XRF spectra from equation (3) compared with the value obtained from photo-absorption in equation (2). The function used is given here by $I_{XRF}(E) = R\,I'_{XRF}(E)$,

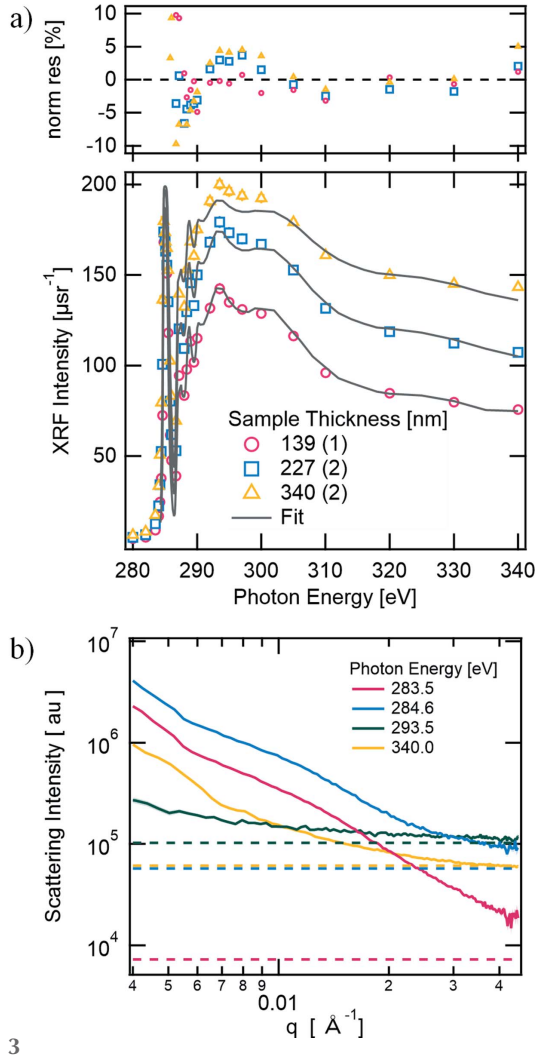

Figure 3
(*a*) $I_{XRF}(E)$ for three polystyrene samples overlaid with fits to equation (2). Intensity has been scaled with the measured relative responsivity reported in Section 4 and is presented in units of sterad^{-1}. Intensity has been processed according to equation (2) and is presented in units of (ADU nA^{-1}). Thicknesses were measured when the sample was rotated by 45° so the true thickness is lower by a factor of $\sqrt{2}$. The top graph of (*a*) presents the normalized residue (norm res) as discussed in the main text. (*b*) RSOXS intensity reported by the CCD detector for a single polystyrene sample (t = 227 nm). Dashed lines represent the XRF background from the measurements in part (*a*).

where R is the relative detector responsivity in units of nA ADU^{-1} and $I_{XRF}(E)$ and $I'_{XRF}(E)$ are defined in equations (2) and (3), respectively. Results from fitting this one parameter to our three samples are presented as the gray lines in Fig. 3(*a*). From this analysis we calculate the relative responsivity of the current detectors at beamline 11.0.1.2 to be $R = (1.73 \pm 0.12) \times 10^{-9}$ nA ADU^{-1}. This value was averaged over the three measured samples and the uncertainty combines the standard deviation of our direct beam measurement in quadrature with the variation determined by the Levenberg–Marquardt fitting algorithm used. The unusual order of magnitude found in our calibration factor is due to an implicit conversion of the current measured by the photodiode into the number of photons in our incident flux. If we explicitly include a conversion of the charge of an electron ($e = 1.602 \times 10^{-9}$ nC) into number of photons, our calibration factor would result in a value of $R = 1.08 \pm 0.07$ ADU^{-1} s^{-1}.

The residues from each sample are represented as a percentage of the measured data and more readily how beam damage impacts our fit results. Below 291 eV, in the π^* manifold, our measured photo-absorbance overestimates the XRF intensity, and above 291 eV, the σ manifold, our fits underestimate the measured intensity. This follows exactly what we expect from increased beam damage following our photo-absorption measurement – a decrease in the XRF from low-energy resonances, and an increase in XRF from high-energy resonances (Wang *et al.*, 2009). However, we note that the uncertainty in our direct beam measurement is still greater than the variation from our calculated values of R for each sample.

One drawback to this method is that the $C_{K\alpha}$ emission band only emits photons with $E_{XRF} = 277$ eV and does not directly measure the energy dependence of R. We can approximate this effect by assuming that each detector will produce an extra electron per incident photon when the energy increases by an amount equal to the bandgap of the detector material. Our relative responsivity then becomes $R(E) = (1.08 \pm 0.07)[1 + g_{PD}/g_{CCD}(E - E_{XRF})/E_{XRF}]$, where g_{PD} is the bandgap for the photodiode [1.43 eV for GaAs (Streetman & Banerjee, 2000)] and g_{CCD} is the bandgap for the CCD [1.14 eV for Si (Streetman & Banerjee, 2000)]. With our current levels of uncertainty as a result of direct beam stability, a significant change in $R(E)$ will not occur unless measuring with photon energies above approximately 290 eV. Many RSOXS measurements over the carbon edge occur well below this photon energy and it may be unnecessary to apply an energy correction until uncertainty in the measurement improves. Ultimately, it will be important to further refine this approximation in the future and calibration at other low-Z elemental edges will require an alternative calibrant sample.

5. Best practice procedure to calibrate the instrument

For an RSOXS user to apply the methods outlined herein, several considerations must be briefly discussed. The specific experimental procedures for absolute intensity calibration can be summarized as follows:

(1) Fabrication of a calibration sample that will fluoresce at the elemental edge under investigation.

(2) $I_{CF}(E)$ is measured for the nominal incident flux on a photodiode prior to XRF detection.

(3) $A(E)$ is measured for the calibration sample while rotated to 45° with respect to the path of the incident X-ray beam.

(4) $I'_{XRF}(E)$ is then measured on the area detector while set up in the geometry outlined in Fig. 2 and images are reduced according to equation (3). (Note that this requires measuring the signal of an additional blank substrate without the thin film calibration sample on it.)

(5) The resulting $I'_{XRF}(E)$ spectrum is fit according to equation (2) and R is determined.

Several options exist in picking a calibration sample and can be left up to the user. Our choice in selecting a thin film of polystyrene was motivated by several factors. First, the relative availability and easy processability of the polymer make it ideal as a calibrant that does not require any advanced equipment to fabricate. The sharp resonance at 285.1 eV also allows it to double as an energy calibrant and both calibrations can be run simultaneously. When choosing a sample, we recommend looking for a stable material that has some degree of radiation resistance, but this method does allow for some choice on what the user has available. One final consideration is in choosing a material with minimal intrinsic scattering cross-section. Pure polystyrene is excellent for this as it has few density variations, no crystallinity, and can be cast with little surface roughness.

The full suite of measurements required for this calibration are facile, making this a technique suitable for all users. We recommend that R is calculated at the start of any beam time where absolute intensity may be required as our reported value of R may drift as the detectors age and contaminants may build up on their active elements reducing their overall efficiency or if detectors are swapped out by beamline staff. CCD detector readout amplifier settings can also be changed, changing the apparent calibration. Fortunately, the steps that we have outlined for a single calibration take approximately 30 min and could be further reduced by either measuring fewer energies or reducing dwell time.

6. Verification of absolute scattering intensity

In order to confirm that we have achieved a calibration for absolute intensity we turn to measure the Flory–Huggins interaction parameter, χ, between polystyrene and poly(methyl methacrylate). The model employed here was originally developed by Leibler (Leibler, 1980) and has been used extensively in the past to measure the interaction parameter of polymers in phase-mixed copolymer melts. Here, we note that the model dependence on χ is directly related to both the shape and intensity of the copolymer scattering, and without properly calibrating the absolute intensity it is not possible to determine χ. The resonant differential scattering cross section for a two-phase system is given by

$$\frac{d\Sigma}{d\Omega}(q, E) = \frac{4\pi V}{\lambda^4} \left|\Delta n_{AB}(E)\right|^2 S(q), \quad (4)$$

where V is the sample volume, λ is the X-ray wavelength, $\Delta n_{AB}(E)$ is the difference in complex index of refraction between the two materials [previously determined for polystyrene and poly(methyl methacrylate) (Ferron *et al.*, 2017)], and $S(q)$ is the structure factor that describes the scattering morphology. The structure factor from an incompressible, phase-mixed block copolymer is given by (Bates & Hartney, 1985)

$$S(q) = N\left[F(q) - 2\chi N\right]^{-1}, \quad (5)$$

where χ is the Flory–Huggins interaction parameter and N is the degree of polymerization. In this study, χ is normalized to a standard reference volume equivalent to the weighted average between block volumes as done in related experiments (Russell *et al.*, 1990). The function $F(q)$ is given by

$$F(q) = \frac{D(R_g)}{D(R_{g1})\,D(R_{g2}) - \frac{1}{4}\left[D(R_g) - D(R_{g1}) - D(R_{g2})\right]^2}, \quad (6)$$

where $D(x)$ is the Debye scattering function, and the radius of gyration $R_{gi}^2 = N_i b_i^2/6$ is defined by the degree of polymerization of the ith block N_i, and the statistical segment length, b_i^2, with $R_g^2 = R_{g1}^2 + R_{g2}^2$. Polydispersity is incorporated into the model following previously established methods (Sakamoto & Hashimoto, 1995). The only unknown parameters within the above model is the interaction parameter, χ, and the statistical segment length b, which will be assumed to be equal for both blocks (Russell *et al.*, 1990). Conveniently, both unknowns can be independently determined from a scattering profile as they govern different morphological properties to be discussed later.

Fig. 4(*a*) gives the temperature-dependent RSOXS for our model block copolymer measured at E = 284.8 eV in order to maximize material contrast in this weakly scattering sample. Each profile exhibits a single broad peak located at q = 0.041 Å^{-1} with no evidence of higher-order reflections. As the samples are heated, the subsequent decrease in scattering intensity and increase in feature width is characteristic of a phase-mixed block copolymer that undergoes a reduction in interaction strength with increasing temperature (Russell *et al.*, 1990). The copolymer used in this study was selected for its low overall degree of polymerization to ensure that it remains in the weakly segregated regime where our model is valid (χN < 10.5) (Bates & Fredrickson, 1990). Unfortunately, the thin film nature of the measured samples caused a sloping background signal that originates from surface scattering. To account for this added surface scattering, we include a power law decay in our model given by $I_{bkg} = A\exp(-p)$.

Model fits are superimposed onto the experimental data in Fig. 4 and the list of fit parameters are given in Table 1. From our fits we determined that the statistical segment length for our copolymer is b = 6.66 Å and increases slightly with temperature. This value is in good agreement with previous studies (Russell *et al.*, 1990). The χ parameter is expected to change with temperature and is recorded in Fig. 4(*b*). The temperature dependence of χ can be represented in terms of entropic and enthalpic contributions that takes the form $\chi(T) = \chi_s + \chi_H/T$ (Bates & Fredrickson, 1990; Zhao *et al.*, 2008). From a linear fit to our extracted χ parameters we can calculate $\chi(T)$ with $\chi_s = 0.0183 \pm 0.0003$ and $\chi_H = 7 \pm 1$. Much like previous measurements of these polymers, the entropic component (χ_s) is significantly larger than the enthalpic contribution (χ_H/T) over the temperature range investigated (Russell *et al.*, 1990; Zhao *et al.*, 2008). We can compare the magnitude of $\chi(T)$ with previous measurements using this scattering model and we find our results to be comparable and within error of these previous investigations (Zhao *et al.*, 2008). It is interesting to note that the measurement conducted here was accomplished on a copolymer as received

Table 1
Parameters from the fits in Fig. 4(*a*).

Temperature	b (Å)	χ	A	p
120°C	6.66 (1)	0.036 (1)	1.51 (4)	−2.75 (2)
140°C	6.67 (1)	0.035 (1)	0.20 (1)	−3.8 (1)
160°C	6.79 (1)	0.034 (1)	4 (1) × 10^{-4}	−7.3 (2)

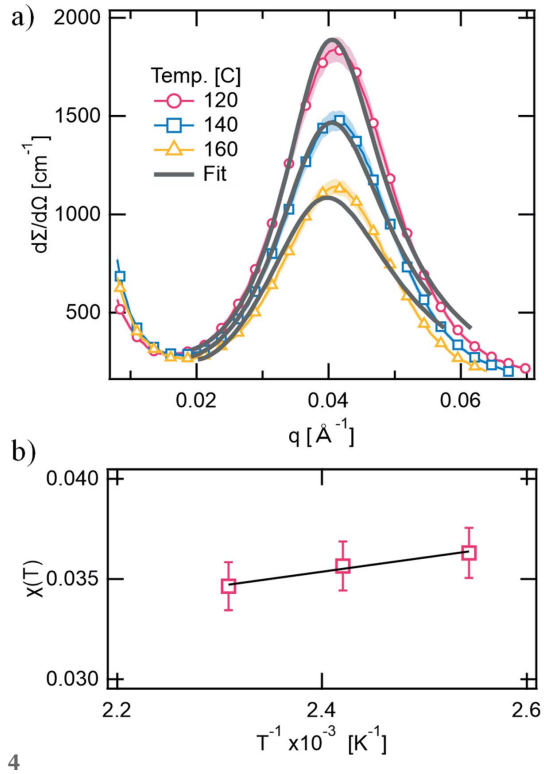

Figure 4
(*a*) Temperature-dependent RSOXS profiles of copolymer scattering as described in the text. Intensity has been scaled to an absolute unit by the responsivity calculated in Section 4. Error is represented by the shaded region and was calculated by combining the profile standard error (as calculated from *NIKA*) with uncertainty in the thickness measurement. Thickness was measured from the photo-absorption and was determined to be 29 ± 1 nm. Gray lines are profile fits to equation (4) with all relevant parameters given in Table 1. (*b*) Extracted χ parameters from the fits in part (*a*). Error is calculated from the Levenberg–Marquardt algorithm used in fitting. The black line is a linear fit as discussed in the main text.

from a manufacturer and required no chemical modifications to increase contrast that may be required for small-angle neutron scattering. This can be beneficial as isotopic labeling has been shown in the past to alter the measured interaction parameter (Russell, 1993).

It is important to reiterate here that the intensities of these RSOXS measurements are independently calibrated from our polystyrene reference film. Without a successful calibration, the model used in this study is not nearly as effective as when the χ parameter is convoluted with the total intensity. These results point to both the confirmation of an absolute intensity and effectiveness of using XRF as an intensity calibrant at the carbon edge. We believe that the simplicity of the methods outlined here gives users an opportunity of calibrating RSOXS data to an absolute intensity and improve the quantitative output from their measurements.

7. Conclusion

In this article we have outlined the methodology to convert a previously parasitic background signal found in RSOXS measurements to a fundamental calibration for absolute scattering intensity. By measuring the XRF from a thin polystyrene film we determined the relative responsivity between the scattering and direct beam detectors at beamline 11.0.1.2 at the ALS. We have outlined the necessary steps for a potential user to apply our technique and discussed requirements and challenges. Verification of an absolute intensity was carried out by measuring the Flory–Huggins interaction parameter between two polymers using an established scattering model that requires absolute intensity. The methods outlined here are presented to help improve the overall effectiveness and scientific output of RSOXS measurements as it gains a wider user base and expands to new topics in soft matter.

Acknowledgements

This research used resources of the Advanced Light Source, which is a DOE Office of Science User Facility under contract No. DE0-AC02-05CH11231.

Funding information

Financial support for T. Ferron, D. Grabner, and B. A. Collins was provided by the US Department of Energy, Office of Science, Basic Energy Sciences, Early Career Research Award number DE-SC0017923.

References

Ade, H. & Hitchcock, A. P. (2008). *Polymer*, **49**, 643–675.
Allen, A. J., Zhang, F., Kline, R. J., Guthrie, W. F. & Ilavsky, J. (2017). *J. Appl. Cryst.* **50**, 462–474.
Bates, F. & Fredrickson, G. H. (1990). *Annu. Rev. Phys. Chem.* **41**, 525–557.
Bates, F. S. & Hartney, M. A. (1985). *Macromolecules*, **18**, 2478–2486.
Bearden, J. A. (1967). *Rev. Mod. Phys.* **39**, 78–124.
Carpenter, J. H., Hunt, A. & Ade, H. (2015). *J. Electron Spectrosc. Relat. Phenom.* **200**, 2–14.
Collins, B. A. & Ade, H. (2012). *J. Electron Spectrosc. Relat. Phenom.* **185**, 119–128.
Collins, B. A., Li, Z., Tumbleston, J. R., Gann, E., McNeill, C. R. & Ade, H. (2013). *Adv. Energy Mater.* **3**, 65–74.
Cui, Y., Yao, H., Zhang, J., Zhang, T., Wang, Y., Hong, L., Xian, K., Xu, B., Zhang, S., Peng, J., Wei, Z., Gao, F. & Hou, J. (2019). *Nat. Commun.* **10**, 2515.
Dreiss, C. A., Jack, K. S. & Parker, A. P. (2006). *J. Appl. Cryst.* **39**, 32–38.
Feng, L., Chen, J., Mukherjee, S., Sangwan, V. K., Huang, W., Chen, Y., Zheng, D., Strzalka, J. W., Wang, G., Hersam, M. C., DeLongchamp, D., Facchetti, A. & Marks, T. J. (2020). *ACS Energy Lett.* **5**, 1780–1787.
Ferron, T., Pope, M. & Collins, B. (2017). *Phys. Rev. Lett.* **119**, 167801.
Gann, E., Young, A. T., Collins, B. A., Yan, H., Nasiatka, J., Padmore, H. A., Ade, H., Hexemer, A. & Wang, C. (2012). *Rev. Sci. Instrum.* **83**, 045110.
Guinier, A. & Fournet, G. (1955). *Small-Angle Scattering of X-rays.* New York: John Wiley & Sons.
Henke, B. L., Gullikson, E. M. & Davis, J. C. (1993). *At. Data Nucl. Data Tables*, **54**, 181–342.
Hinde, E., Thammasiraphop, K., Duong, H. T. T., Yeow, J., Karagoz, B., Boyer, C., Gooding, J. J. & Gaus, K. (2017). *Nat. Nanotechnol.* **12**, 81–89.
Hubbell, J. H., Trehan, P. N., Singh, N., Chand, B., Mehta, D., Garg, M. L., Garg, R. R., Singh, S. & Puri, S. (1994). *J. Phys. Chem. Ref. Data*, **23**, 339–364.
Ilavsky, J. (2012). *J. Appl. Cryst.* **45**, 324–328.
Krause, M. O. & Oliver, J. H. (1979). *J. Phys. Chem. Ref. Data*, **8**, 329–338.
Leibler, L. (1980). *Macromolecules*, **13**, 1602–1617.
Liang, Z., Li, M., Wang, Q., Qin, Y., Stuard, S. J., Peng, Z., Deng, Y., Ade, H., Ye, L. & Geng, Y. (2020). *Joule*, **4**, 1278–1295.
Orthaber, D., Bergmann, A. & Glatter, O. (2000). *J. Appl. Cryst.* **33**, 218–225.
Rivnay, J., Inal, S., Collins, B. A., Sessolo, M., Stavrinidou, E., Strakosas, X., Tassone, C., Delongchamp, D. M. & Malliaras, G. G. (2016). *Nat. Commun.* **7**, 11287.
Roe, R.-J. J. (2000). *Methods of X-ray and Neutron Scattering in Polymer Science.* New York: Oxford University Press.
Russell, T. Jr, Hjelm, R. P. & Seeger, P. A. (1990). *Macromolecules*, **23**, 890–893.
Russell, T. P. (1993). *Macromolecules*, **26**, 5819.
Sakamoto, N. & Hashimoto, T. (1995). *Macromolecules*, **28**, 6825–6834.
Spalla, O., Lyonnard, S. & Testard, F. (2003). *J. Appl. Cryst.* **36**, 338–347.
Stöhr, J. (1992). *NEXAFS Spectroscopy.* Springer US.
Streetman, B. G. & Banerjee, S. (2000). *Solid State Electronic Devices.* Englewood Cliffs: Prentice Hall.
Wang, J., Morin, C., Li, L., Hitchcock, A. P., Scholl, A. & Doran, A. (2009). *J. Electron Spectrosc. Relat. Phenom.* **170**, 25–36.
Wignall, G. D. & Bates, F. S. (1987). *J. Appl. Cryst.* **20**, 28–40.
Ye, L., Hu, H., Ghasemi, M., Wang, T., Collins, B. A., Kim, J. H., Jiang, K., Carpenter, J. H., Li, H., Li, Z., McAfee, T., Zhao, J., Chen, X., Lai, J. L. Y., Ma, T., Bredas, J. L., Yan, H. & Ade, H. (2018). *Nat. Mater.* **17**, 253–260.
Zhang, F., Ilavsky, J., Long, G. G., Quintana, J. P. G., Allen, A. J. & Jemian, P. R. (2010). *Metall. Mater. Trans. A*, **41**, 1151–1158.
Zhang, S. (2003). *Nat. Biotechnol.* **21**, 1171–1178.
Zhang, W., Shi, Y., Chen, Y., Ye, J., Sha, X. & Fang, X. (2011). *Biomaterials*, **32**, 2894–2906.
Zhao, Y., Sivaniah, E. & Hashimoto, T. (2008). *Macromolecules*, **41**, 9948–9951.